Electronic Supporting Information

Zone-Specific Crystallization and a Porosity-Directed Scaling Marker for the Catalytic Efficacy of Au–Ag Alloy Nanoparticles

Sandip Kumar De,[†] Subrata Mondal,[†] Abhijit Roy,[‡] Sourabh Kumar,[§] Manabendra Mukherjee,[⊥] Sudeshna Das Chakraborty,[†] Pintu Sen,[∥] Biswarup Pathak,[§] Biswarup Satpati,[‡] Mrinmay Mukhopadhyay,[‡] Dulal Senapati[†]*

[†]Chemical Sciences Division & [§]Surface Physics and Materials Science Division, HBNI, Saha Institute of Nuclear Physics, 1/AF Bidhannagar, Kolkata 700064, India

[§]Discipline of Chemistry, Discipline of Metallurgy Engineering and Materials Science, IIT Indore, Indore 453552, India

[⊥]Surface Physics and Materials Science Division, Saha Institute of Nuclear Physics, 1/AF Bidhannagar, Kolkata 700064, India

[∥] Variable Energy Cyclotron Centre, 1/AF Bidhannagar, Kolkata 700064, India

KEYWORDS: Au–Ag alloy nanoparticles, Kirkendall effect, d-orbital spacing, nanoporous ligaments, tensile strain, electrocatalysis

*Email: dulal.senapati@saha.ac.in

	Content
	Kirkendall Effect
Figure S1	Plasmonic nature of individual HNPrs from UV-Vis-NIR spectra.
Figure S2	Histogram of each HNPr size distribution
Figure S3	XRD of $HNPr_{250}$, $HNPr_{50,}$ and $HNPr_{2k}$.
Figure S4	Fitted XRD curve at {111} facet.
Figure S5a-5c	EDX spectra and STEM image for $HNPr_{100,}$ $HNPr_{500,}$$HNPr_{3K}$.
Figure S6	XPS survey spectrum of $HNPr_{100}$.
Figure S7	Thickness plot of $HNPr_{250}$.
Figure S8	Representative twin boundaries on the $HNPr_{250}$ surface.
Figure S9	Appearance of GB on different HNPr surface.
Figure S10	(a) Presentation of $HNPr_{250}$ for the calculation of Surface Grain Boundary Density (SGBD) (b) edge length and cavity length determination of $HNPr_{250}$.
Figure S11	Equivalent circuit of the Nyquist Plot.

Figure S12	SERS spectra of different HNPr with CV (crystal violet) as the Raman reporter with excitation wavelength at 532 nm.

Kirkendall Effect

Kirkendall effect is a metallurgical process to produce hollow nanostructures by applying the differential diffusion rates of two metallic species with appropriate control over the shape and sizes.[1] The intermetallic diffusion occurs within a bimetallic species where standard reduction potential is different for two metallic species and the galvanic reaction takes place. However, the reaction is not simply electrochemical dissolution as confirmed by Smith et al.[2], where they found that when Ag nanoparticles are exposed to Au^{3+}, the scattering intensity of the individual nanoparticles decreases nonlinearly after few seconds due to formation of voids. The rate of void formation (r) was estimated as[2]:

$$r \propto exp \frac{-16\pi\gamma^3 v^2}{3kTg^2}$$

Where r is the rate, γ is the surface tension between the Ag phase and the solution, g is the free energy of formation of a single Ag vacancy and *v* is the volume of the vacancy.

Thus the galvanic replacement is coupled with void formation to form cage-like structures[3] in Au–Ag alloy nanoparticle. The size of a critical void was also estimated by smith et al.[2] is around 20 atomic sizes.

So by controlling the galvanic replacement at room temperature and modified reaction condition, the Kirkendall effect can be introduced to generate hollow nanostructures in bimetallic Au–Ag nanostructures.

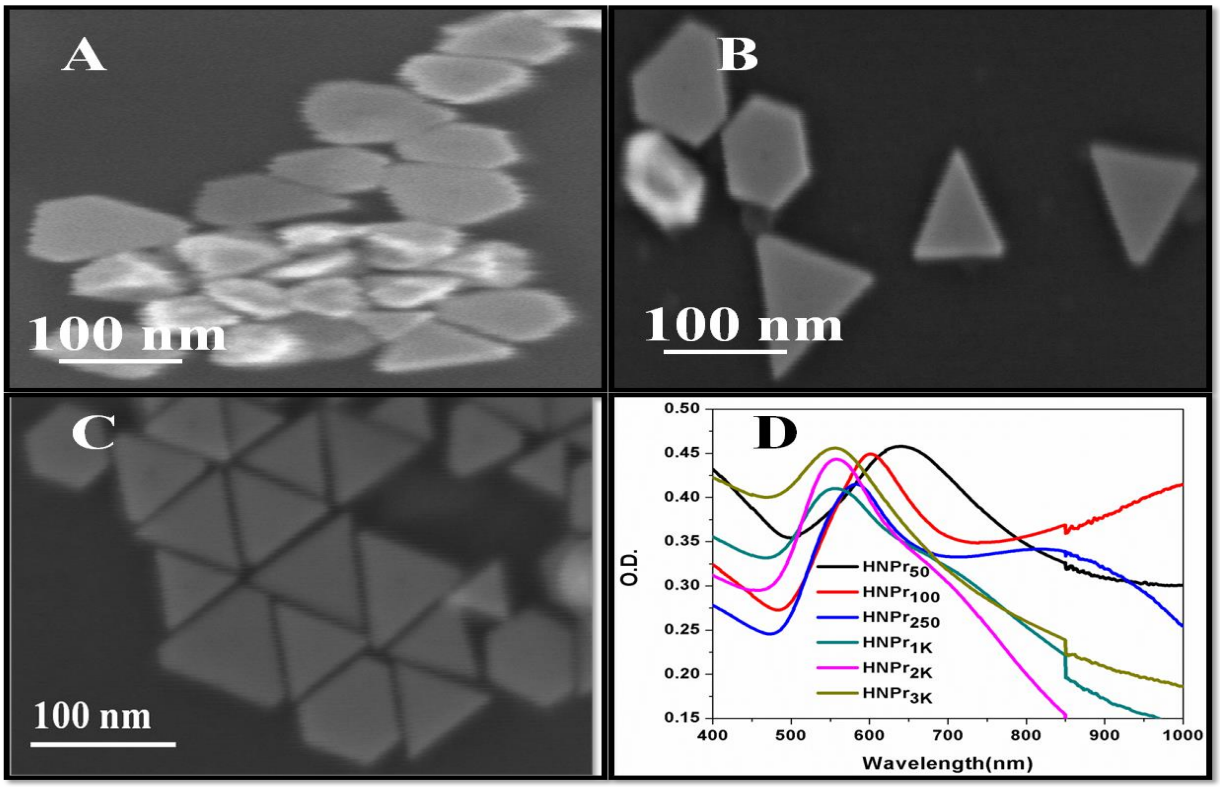

Figure S1: (A), (B) and (C) SEM images of $HNPr_{250}$ with $HAuCl_4.3H_2O$ addition rate (second step of seeded growth) of 1mL/min, 2mL/min and 3mL/min respectively. (D) Absorption spectra of different HNPrs.

It is clear that if we deviate the addition rate of $HAuCl_4.3H_2O$ in the second step of seeded growth from 2mL/min then the produced HNPrs distort in shape. Distortion in size and shape are clearly visible from Figures A and B where we have used the addition rate of $HAuCl_4.3H_2O$ as 1mL/min and 3mL/min respectively. Due to the similarity in the absorption pattern between $HNPr_{250}$ & $HNPr_{500}$ and to avoid the congestion we have not included the spectrum of $HNPr_{500}$ in figure D.

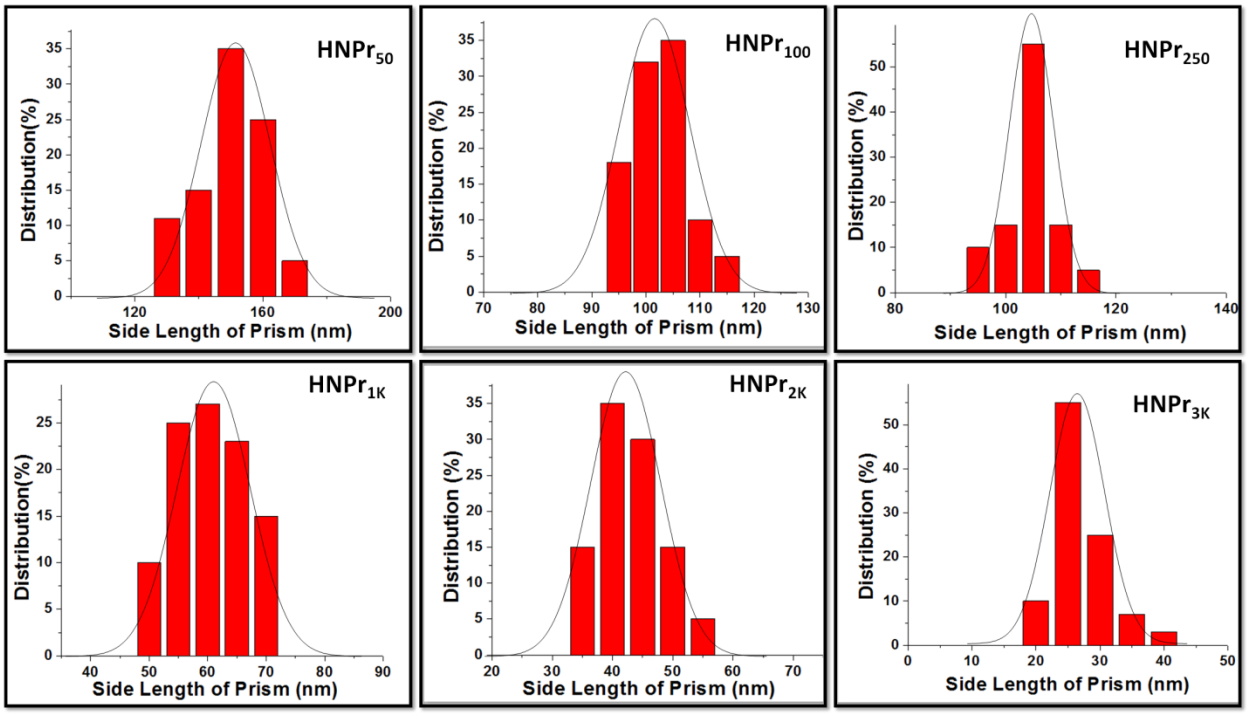

Figure S2: Histogram of size distribution for each HNPr. 100 TEM frames have been considered for each HNPr to calculate their average edge length.

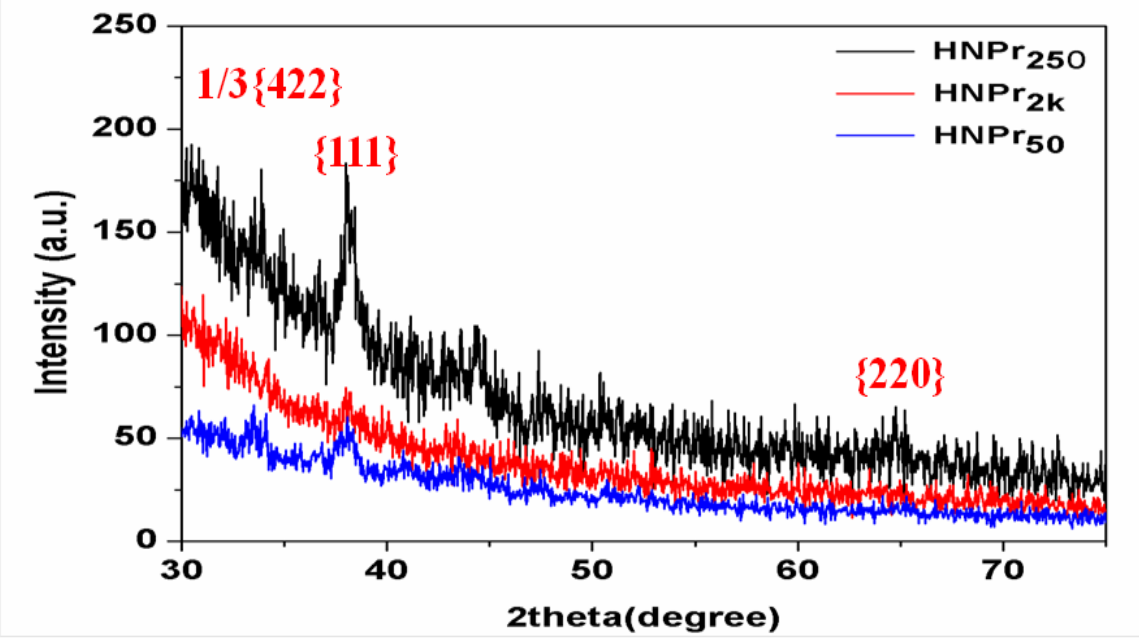

Figure S3: XRD pattern of $HNPr_{50}$, $HNPr_{250}$, and $HNPr_{2K}$.

Recorded XRD pattern confirms the presence of {111} at $2\theta \approx 38.25^0$, 1/3{422} at $2\theta \approx 34.00^0$, and {220} at $2\theta \approx 65.00^0$ facets in $HNPr_{250}$, $HNPr_{50}$ and $HNPr_{2K}$. The broadening of the XRD curve in $HNPr_{250}$ at {111} crystal facet ($2\theta \approx 38.25^0$) compared to that of $HNPr_{50}$ and $HNPr_{3K}$ is owing to the lattice strain, which arises due to the (i) prevention of motion of dislocation from central porous region to crystalline periphery by grain boundary (ii) appearance of Kirkendall voids during replacement of Ag^0 by Au^{3+} and (iii) various crystal irregularities. The strain (ε) within HNPr can be calculated through the Williamson–Hall isotropic strain model and represented by:

$$\varepsilon = \beta_\varepsilon / 4\tan\theta_{hkl} \quad \text{.....(1)}$$

where {hkl}={111} in this case and β_ε is full-width half maxima[4] for the diffraction peak. We have calculated the strain from XRD data by applying the above equation and it follows the same order as observed for catalytic activity: $HNPr_{250} \approx HNPr_{500} > HNPr_{1K} > HNPr_{2K} > HNPr_{3K} > HNPr_{100} > HNPr_{50}$.

In the case of $HNPr_{250}$, the strain (dimensionless, as it is a ratio of two length unit) calculation is given here. We have fitted the curve at $2\theta \approx 38.25^0$ for $HNPr_{250}$ which is shown below:

where $\beta_\varepsilon = 0.8^0$ (at $2\theta \approx 38.25^0$)

By converting β_ε in radian we can write $\beta_\varepsilon = 0.0139$ radian

Hence, the calculated strain for $HNPr_{250}$ by equation (1) can be expressed as:

$\varepsilon = 0.0139/(4\times\tan 0.33) = .01 = 1\times10^{-2}$. For this equation, we have converted the θ into radian too.

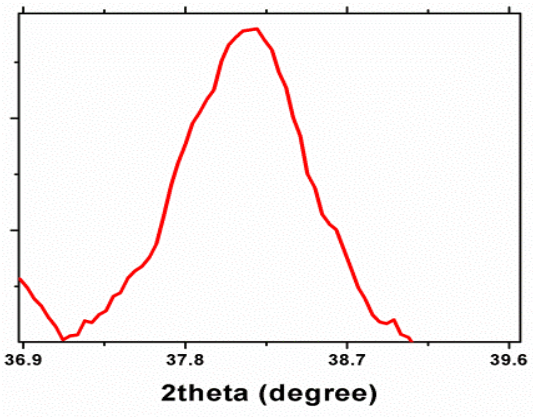

Figure S4: Fitted curve of XRD at {111} facet to calculate the strain.

A similar curve fitting was carried out for other facets in the XRD curve like 1/3{422} and {220}. We then calculate the strain of each HNPr by taking the average of three fitted curves.

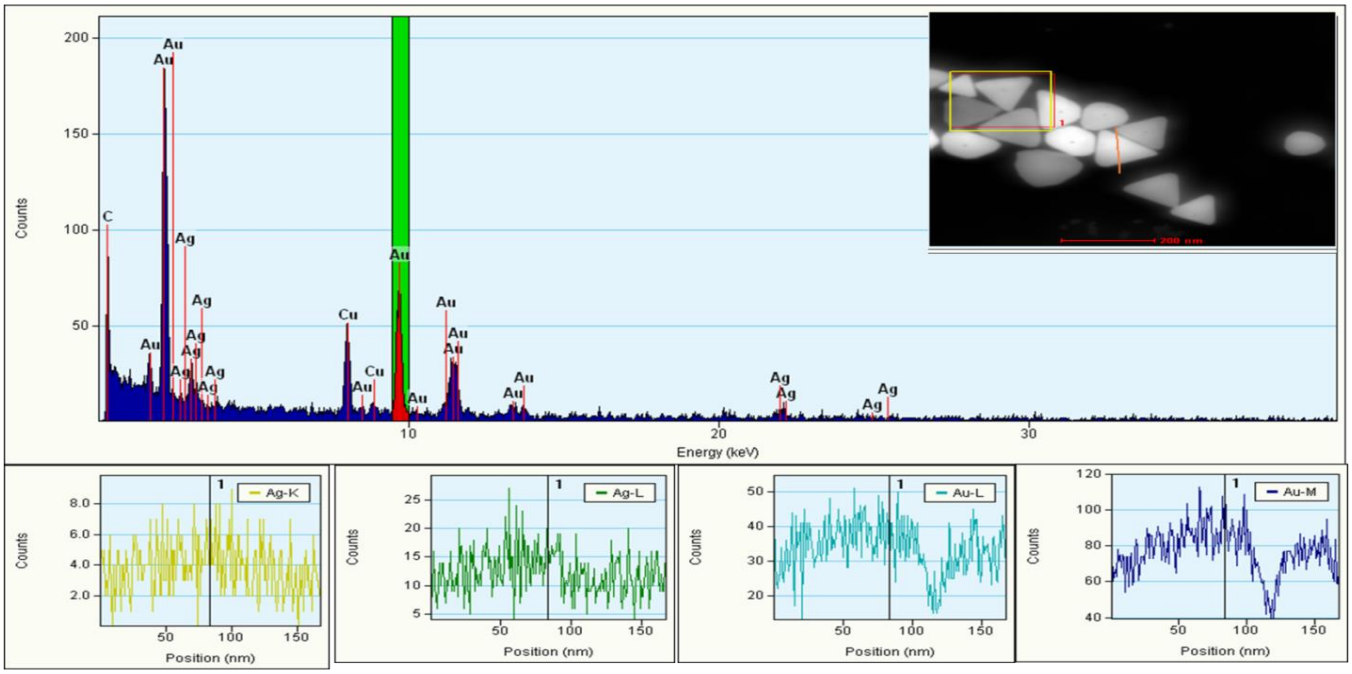

Figure S5a: EDX spectra and HAADF–STEM image of $HNPr_{100}$ for the confirmation of bimetallic (Au–Ag) nature.

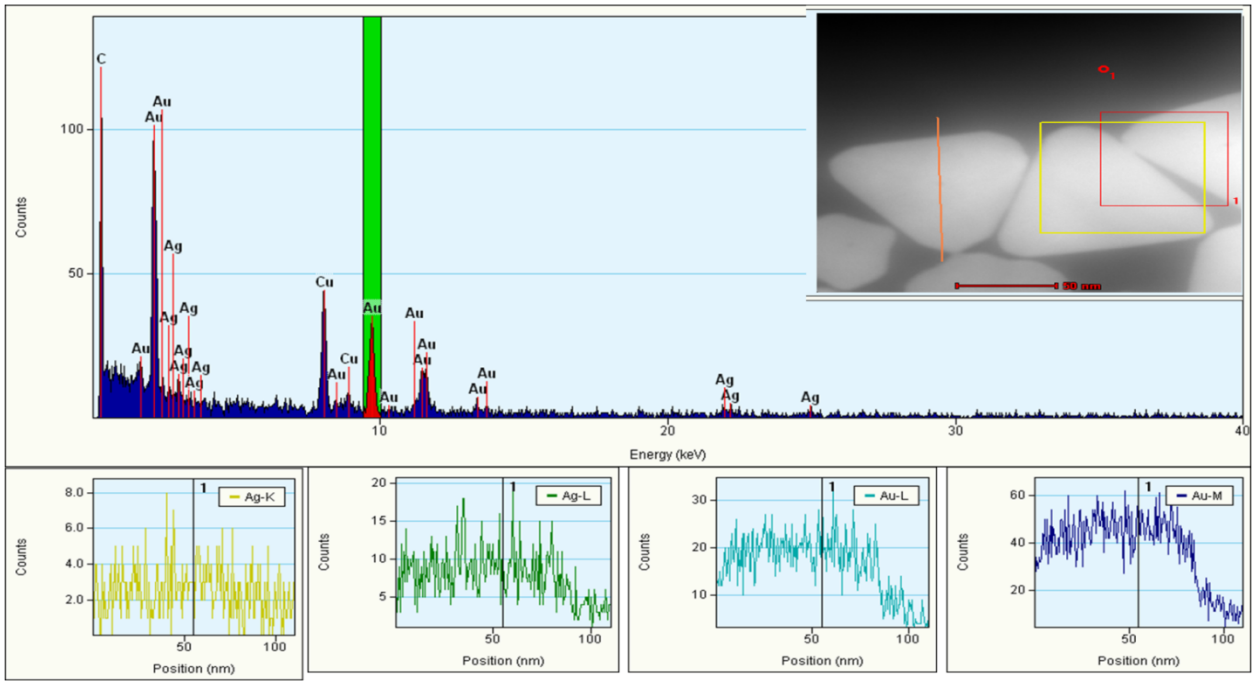

Figure S5b: EDX spectra and HAADF–STEM image of $HNPr_{500}$ for the confirmation of bimetallic (Au–Ag) nature.

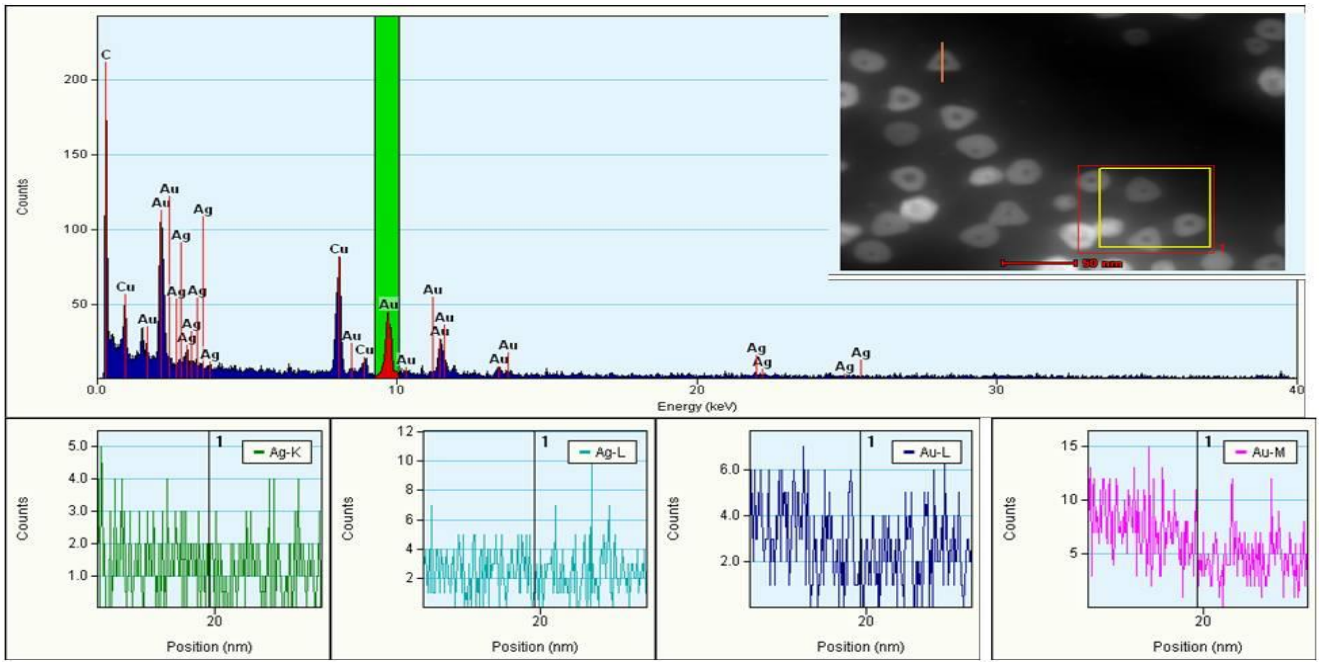

Figure S5c: EDX spectra and HAADF–STEM image of $HNPr_{3K}$ for the confirmation of bimetallic (Au–Ag) nature.

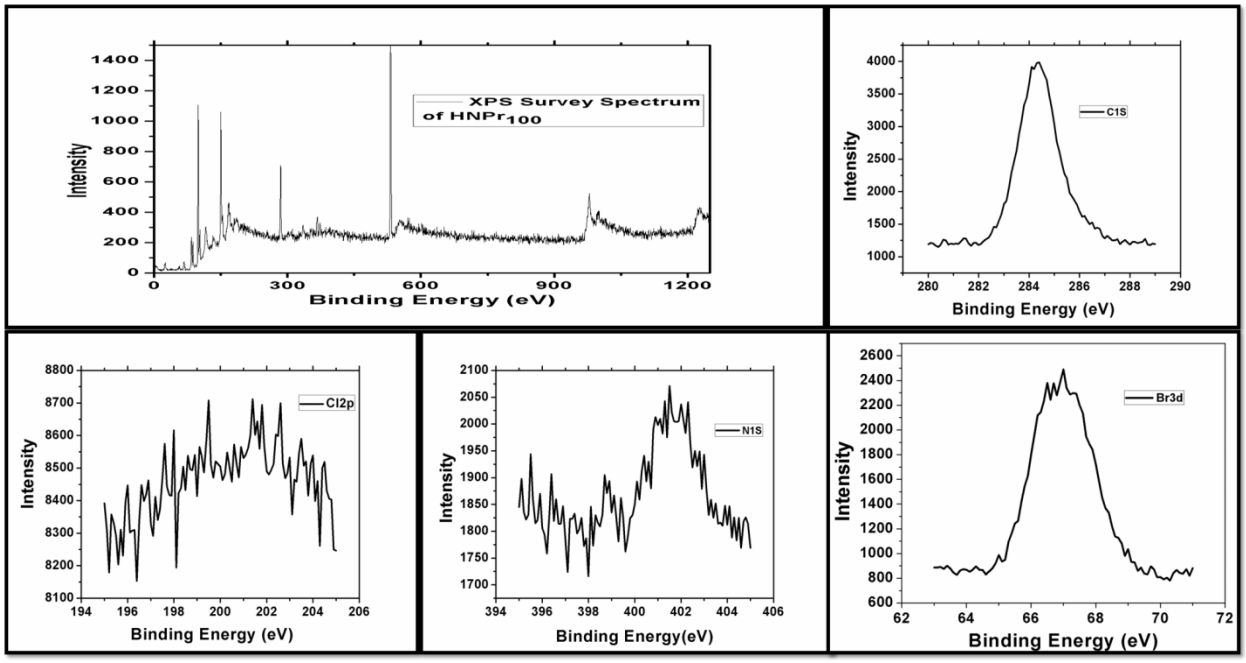

Figure S6: XPS survey spectrum of Cl^-(2p), C(1s) and N(1s) in $HNPr_{100}$ which confirms their presence in the sample.

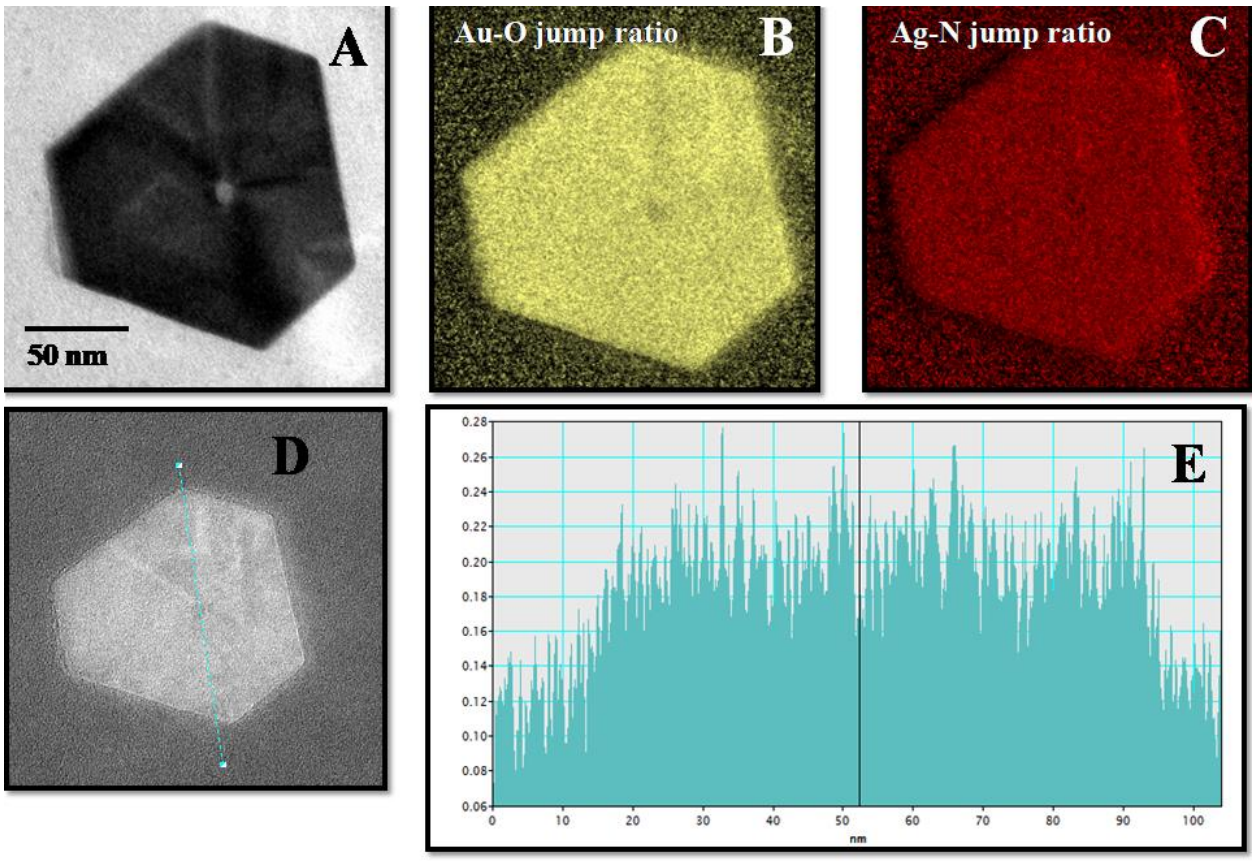

Figure S7: Thickness, as well as elemental mapping of $HNPr_{250}$ where (A) shows the TEM image of a single $HNPr_{250}$, (B) & (C), are the elemental mapping for Au and Ag respectively and the dark region in the central cavity region of Au mapping proves the presence of Ag in large extent compared to Au, (D) high annular dark field image of the single $HNPr_{250}$ with a scanning line through the central cavity in green line, and (E) the corresponding thickness profile for opposite edge-to-edge 100nm scanning.

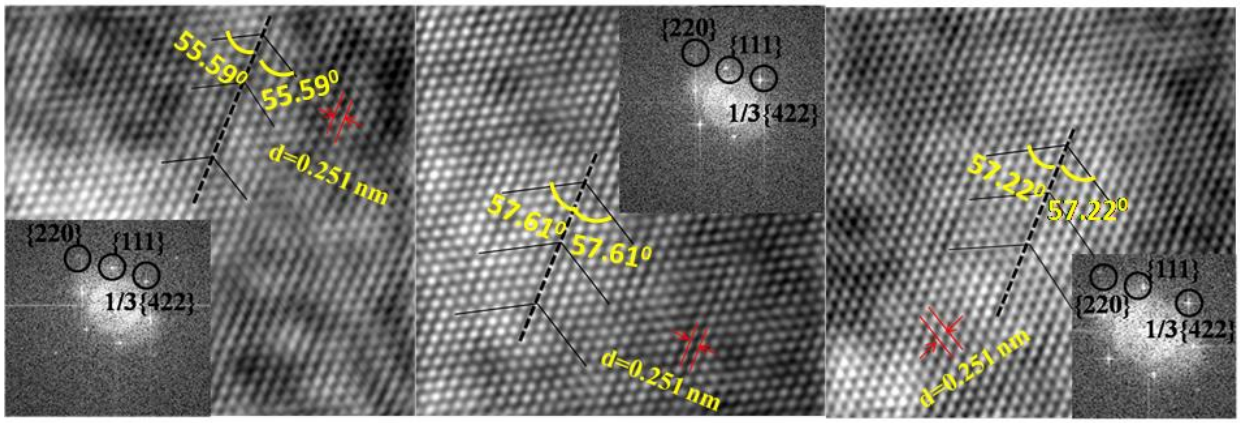

Figure S8: Representative twin boundaries on the $HNPr_{250}$ surface, spotted in three different zones outside the central cavity zone. The twin angle (with reference to the twin boundary) varies in the range of $55–57^0$.

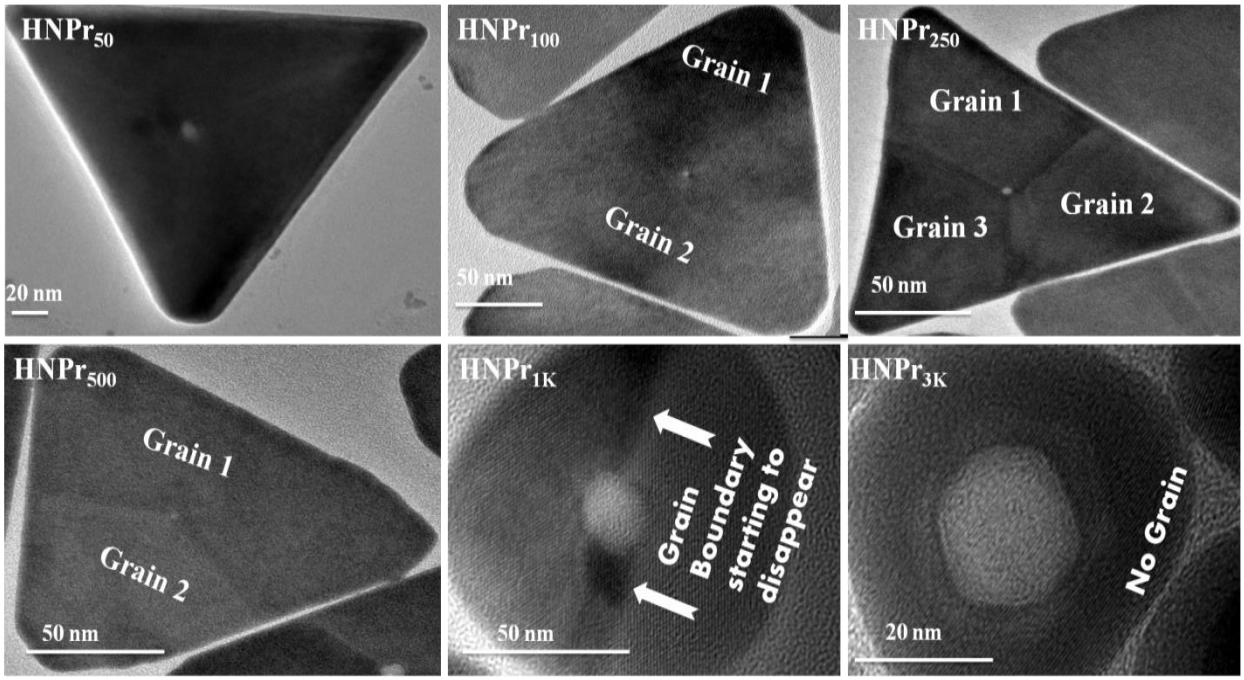

Figure S9. TEM images of the distribution of different grains over individual HNPr surface.

Each grain observed on the crystalline HNPr surface i.e. in the peripheral zone of the central cavity. $HNPr_{50}$ appears almost like a perfect 2D prism with no grains whereas in $HNPr_{100}$ the grains are starting to appear. In $HNPr_{250}$ we have observed a maximum number of GBs which again staring to reduce for $HNPr_{1K}$ and $HNPr_{3K}$ due to the distortion of structures from prism to hollow disc. Thus the alloy formation over the $HNPr_{250}$ surface helps to create multiple GBs, which retards the motion of dislocation from the porous core to the crystalline HNPr surface and creates tensile stress into $HNPr_{250}$ surface. Tensile strain in different HNPrs was calculated before via XRD broadening, which is in agreement with the GB appearance on different HNPr surface. Thus to quantify the contribution of GBs to lattice strain in a more precise way, surface GB density (SGBD) on each HNPr surface has been calculated.

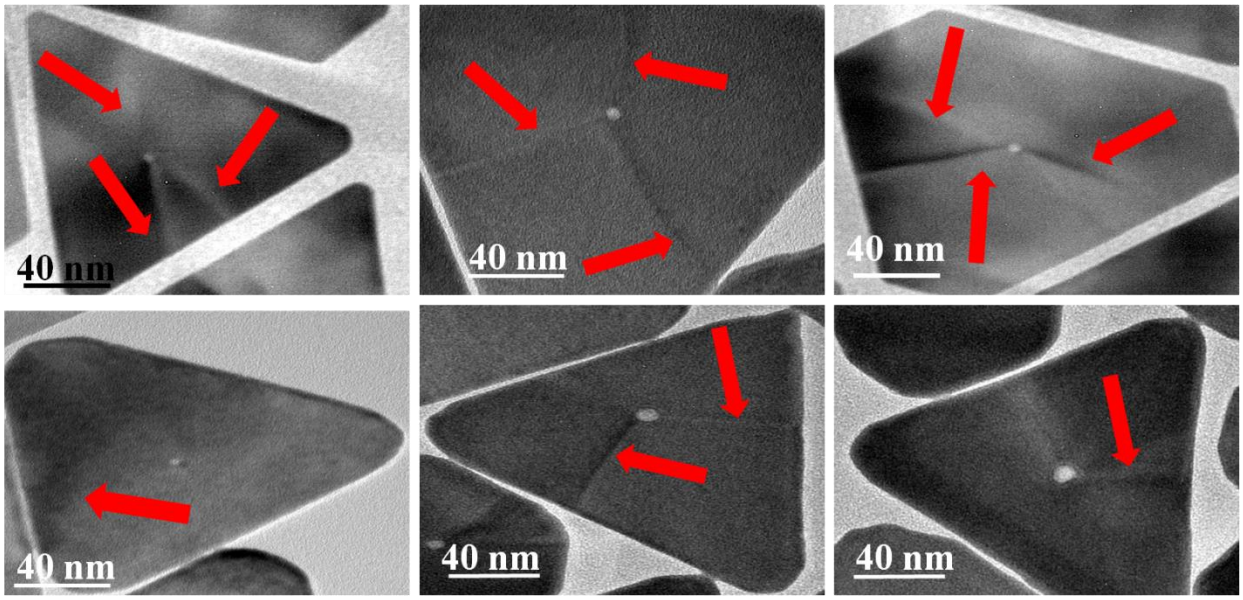

Figure S10(a): Presentation of different $HNPr_{250}$ frames for the calculation of Surface Grain Boundary Density (SGBD).

For the statistical calculation of SGBD, we have selected 100 frames for each individual category. As illustrated in the manuscript, SGBD was calculated by the following formula:

$$C_i = \sum_{i=1}^{i=100} n_i / A_i$$

Where n_i the number of GB and A_i is the surface area of ith HNPr.

We have considered each HNPr as an equilateral triangle and central core as a sphere. Since there is no GB on the central cavity as we have discussed previously, the effective surface area is calculated by subtracting to the central spherical cavity area from the total HNPr area.

$$Ai = \frac{\sqrt{3}}{4} a^2 - \pi r^2$$

Where a is the side length of HNPr and r is the radius of the central cavity.

As an example,

For $HNPr_{250}$ **(Figure S8b)**

$a \approx 105\ nm$ and $r \approx 4.25\ nm$

So $Ai = \{\frac{\sqrt{3}}{4} (105)^2 - \pi * (4.25)^2\}$ nm^2

$= 9491.18\ nm^2$

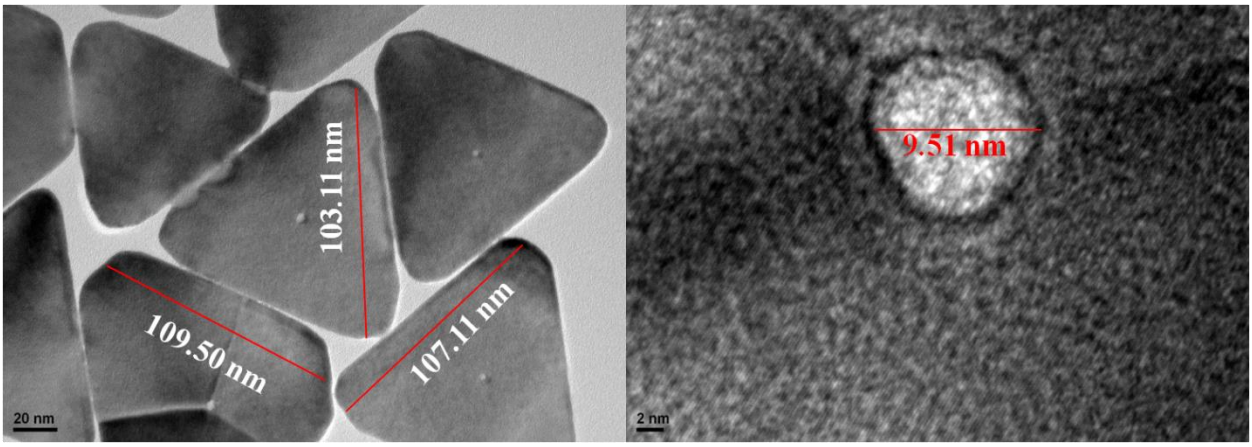

Figure S10(b): Edge length and cavity radius determination in $HNPr_{250}$ by using digital micrograph software.

So if we carry out the approximate calculation of SGBD according to **figure S8a** by counting the number of GBs/ frame and carry out the calculation up to 100^{th} frame,

It appears as:

$$C_i = \frac{3}{9491.18} + \frac{3}{9491.18} + \frac{3}{9491.18} + \frac{1}{9491.18} + \frac{2}{9491.18} + \frac{1}{9491.18} + \cdots \ldots \ldots \ldots \ldots \ldots + \frac{3}{9491.18} (upto\ 100th\ term)$$

$$= 0.00287\ nm^{-2}$$

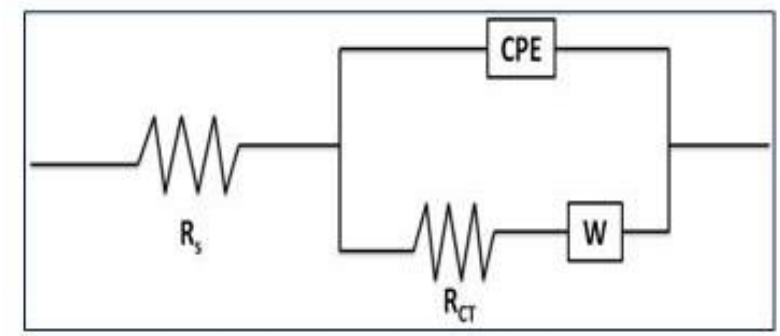

Figure S11: Equivalent circuit for the Nyquist plot.

Parameters of the Circuit:

Rs = Solution resistance

R_{CT} = Charge transfer resistance,

W = Warburg impedance, a kind of resistance to mass transfer, and

CPE = Constant Phase Element which raises due to the double-layer capacitor.

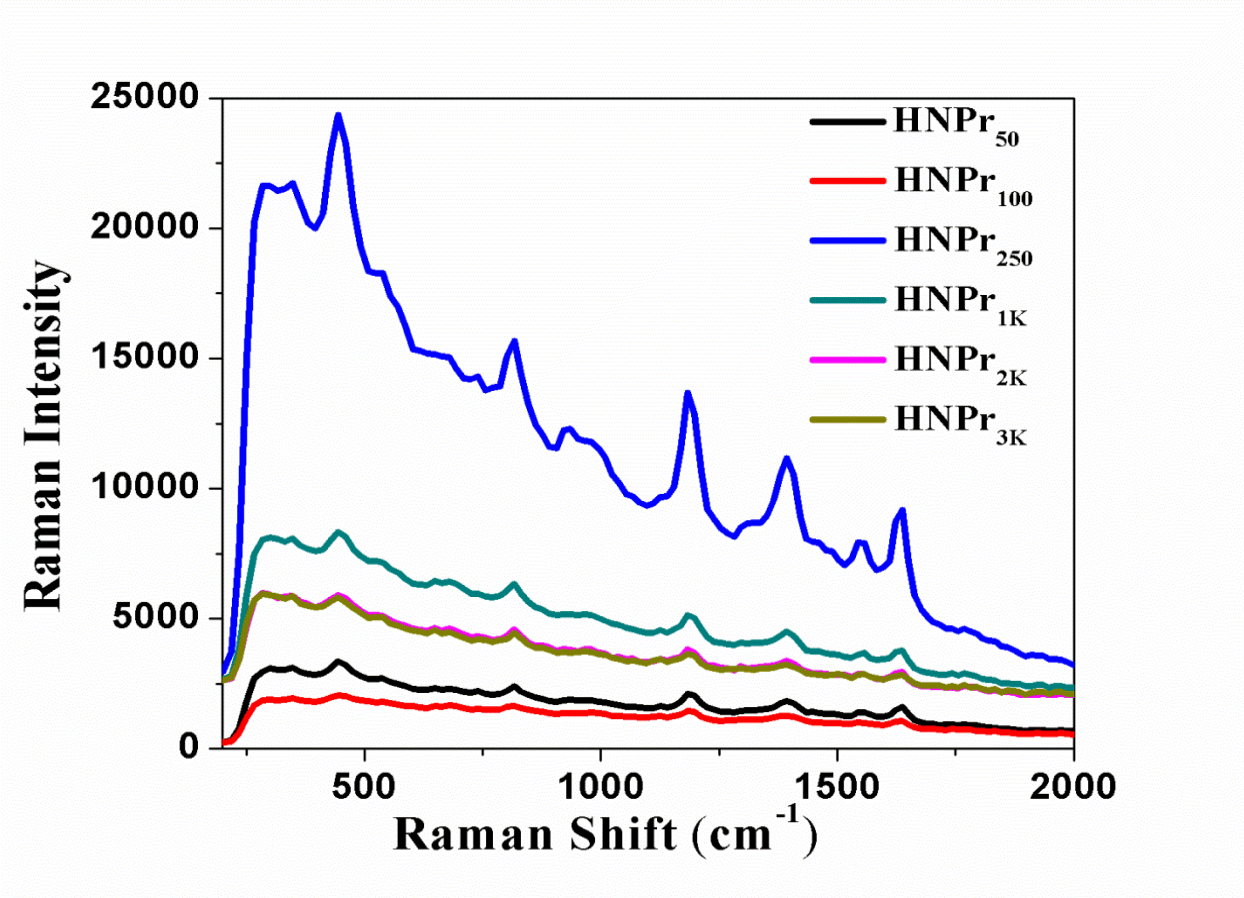

Figure S12: SERS spectra of different HNPr with CV (crystal violet) as the Raman reporter in which $HNPr_{250}$ shows maximum Raman intensity. The result is very much well agreed with our previous arguments. The Raman dye binds to the HNPr surface according to the extent of porosity in the central cavity region.

Besides the porous central cavity region, we have detected several low coordinated atomic islands on the HNPr surface. Recently it has been reported that the formation of nano-islands on nanoporous alloy may result in higher electromagnetic enhancement due to the uniformly distributed hotspot on larger surface area[5]. Therefore, our synthesized pseudo-porous island enriched HNPr is highly SERS active along with enormous catalytic efficiency.

References:

(1) Tianou, H.; Wang, W.; Yang, X.; Cao, Z.; Kuang, Q.; Wang, Z.; Shan, Z.; Jin, M.; Yin, Y. Inflating Hollow Nanocrystals through a Repeated Kirkendall Cavitation Process. *Nat. Commun.* **2017**, *8* (1), 1261.

(2) Smith, J. G.; Yang, Q.; Jain, P. K. Identification of a Critical Intermediate in Galvanic Exchange Reactions by Single-Nanoparticle-Resolved Kinetics. *Angew. Chemie Int. Ed.* **2014**, *53* (11), 2867–2872.

(3) Chee, S. W.; Tan, S. F.; Baraissov, Z.; Bosman, M.; Mirsaidov, U. Direct Observation of the Nanoscale Kirkendall Effect during Galvanic Replacement Reactions. *Nat. Commun.* **2017**, *8* (1), 1224.

(4) Muhammed Shafi, P.; Chandra Bose, A. Impact of Crystalline Defects and Size on X-Ray Line Broadening: A Phenomenological Approach for Tetragonal SnO_2 Nanocrystals. *AIP Adv.* **2015**, *5* (5), 057137.

(5) Huang, J.; He, Z.; He, X.; Liu, Y.; Wang, T.; Chen, G.; Tang, C.; Jia, R.; Liu, L.; Zhang, L.; et al. Island-like Nanoporous Gold: Smaller Island Generates Stronger Surface-Enhanced Raman Scattering. **2017**.